

# Measurement of atomic oxygen densities using TALIF on a dielectric barrier discharge: Insights into the volume above a micro cavity plasma array

David Steuer<sup>1</sup>, Brian Z. Bentz<sup>2</sup>, Kevin Youngman<sup>2</sup>, Henrik van Impel<sup>1</sup>, Marc Böke<sup>3</sup>, Volker Schulz-von der Gathen<sup>3</sup> and Judith Golda<sup>1</sup>

<sup>1</sup>Plasma Interface Physics, Ruhr-University Bochum, D-44801 Bochum, Germany

<sup>2</sup>Sandia National Laboratories, Albuquerque, New Mexico, USA

<sup>3</sup>Experimental Physics II: Physics of Reactive Plasmas, Ruhr-University Bochum, D-44801 Bochum, Germany

E-mail: david.steuer@rub.de

August 2024

**Abstract.** Dielectric barrier discharges, particularly micro cavity plasma arrays, offer significant potential for plasma-catalytic research due to their ability to ignite plasma in direct contact with a catalytic surface, enabling the observation of plasma-surface interactions. A key factor in their application is the generation of reactive species, such as atomic oxygen, within the cavities. These species can interact with both, the surface (e.g., for activation or cleaning) and the gas being treated (e.g., for oxidation). Given the central role of oxygen atoms in plasma catalysis and their use as a model for more complex species, this work investigates the transport of these atoms out of the cavities. Two-photon absorption laser induced fluorescence (TALIF) spectroscopy with picosecond resolution is performed in the volume above the cavities. The results are compared with a basic diffusion model. The reactor operates with a He/O<sub>2</sub> mixture at a flow rate of 1 slm and atmospheric pressure. Densities of up to  $10^{16}$  cm<sup>-3</sup> are measured near the surface. Time-dependent measurements show that, at a distance of 350 μm from the surface, a density equilibrium is reached within less than 3 ms of reactor operation. Decay times due to ozone formation after the reactor is turned off are on a similar scale. Spatially resolved measurements show that the oxygen density decreases exponentially from the surface but remains detectable up to approximately 1 mm above the surface, indicating significant application potential. Variations in the O<sub>2</sub> admixture show a density maximum at 0.4%, confirming previous helium state enhanced actinometry measurements within the cavities.

## 1. Introduction

The conversion of molecular gases, such as volatile organic compounds (VOCs) [1–3], using plasmas is currently a major research focus. A novel approach in this field, plasma catalysis or plasma-assisted catalysis [4–7], combines the unique properties of plasmas with those of conventional heterogeneous catalysts. The goal is to create synergistic effects that can, for example, lower reaction temperatures to enhance energy efficiency or control the selectivity of specific reactions [8]. Atmospheric pressure discharges are ideal for industrial-scale gas conversion or plasma catalysis due to the high flux of reactants to surfaces. A specific type of reactor in this category is the micro cavity plasma array (MCPA) [9]. This reactor consists of a grounded electrode, a dielectric layer, and a powered metal grid, within which thousands of cavities with micrometer-scale diameters are arranged. The reactor is characterized by reproducible operation, where the discharge is confined within the cavities, and each cavity can be described as a dielectric barrier discharge (DBD) [9–11]. This scalable design concept allows the dielectric to be coated with a catalytic layer, placing the discharge in direct contact with this surface, enabling the direct investigation of interactions. Furthermore, the reactor is modular and the components interchangeable, allowing for variations in materials and post-plasma surface diagnostics.

Plasma-catalytic processes are generally very complex due to the multitude of reactions occurring in the gas phase, within the discharge, and on the surface. To disentangle the responsible mechanisms and study their influence on catalysis, a fundamental understanding of the reactor operation is essential. This includes knowledge of the general discharge characteristics [9,10], the electric field [12,13], and surface charges [11].

Oxygen is an excellent model system for understanding the behavior of reactive species. It plays a crucial role in many plasma-catalytic systems, as it is either released during the dissociation of the gases to be converted or actively added to oxidize gases or prevent coking on surfaces. Additionally, the plasma chemical complexity of oxygen systems is relatively limited, often allowing simple models to describe the system adequately. These insights can provide valuable conclusions for other, more complex reactive systems.

In the micro cavity plasma array, the influence of oxygen on the discharge has already been investigated us-

ing helium state-enhanced actinometry (SEA) [14,15]. The results indicate that the reactor can efficiently dissociate oxygen, achieving dissociation rates of up to 100% within the cavities.

However, for practical applications, it is important to understand how many reactive species can exit the cavities to interact with the gas or a surface outside. Investigating the transport mechanisms is also of great importance, here. For example, adding a second surface outside would increase catalytic surface area compared to the cavities alone, which could be expected to improve the conversion efficiency of gases to desired species. This second surface could be exposed to the reactive species only and not to the discharge, allowing use of catalytic surfaces that are not optimized for direct plasma exposure. Finally, understanding of the transport mechanisms could allow to control the flux of reactive species to the second surface by changing its position relative to the array of cavities. Furthermore, it is important to understand to what extent reactive species are transported from cavity to cavity to create possible accumulation effects.

Since there is almost no discharge outside the cavities present, optical emission spectroscopy cannot be applied in these regions. An alternative approach is two-photon absorption laser-induced fluorescence (TALIF) measurements [16–18]. In this method, oxygen atoms are excited by a laser, and a photon is emitted during relaxation. The ground-state density can then be determined by measuring the emission. For determining absolute densities, a noble gas calibration is typically performed [19,20]. The state pair  $O(3p\ ^3P_{1,2,0})$  of oxygen and  $Xe(6p\ '[3/2]_2)$  of xenon is particularly suitable for this, as their excitation wavelengths differ by only about 1.3 nm. The fluorescence signal is shifted by approximately 10 nm, allowing minimal changes to the experimental setup and ensuring nearly identical experimental conditions.

In the case of atmospheric pressure plasmas, picosecond-lasers offer a significant advantage over nanosecond-lasers for TALIF measurements. The shorter pulses make it possible to measure the temporal decay of excited states, typically reduced by quenching at atmospheric pressure to a range of a few nanoseconds, with higher time resolution. This allows the effective lifetimes to be measured directly, providing insights into quenching species [21–23].

The aim of this work is to understand the distribution of atomic oxygen outside the cavities and to de-

scribe the transport and loss processes. To achieve this, TALIF measurements will be conducted, and the results will be compared with a basic diffusion model and with previous measurements [15].

## 2. Experimental Setup

### 2.1. Plasma source

The plasma source used in this work is a micro cavity plasma array (shown in figure 1 (b)). A neodymium magnet (50x15x5 mm) is embedded in a polyetheretherketone (PEEK) carrier and serves as a grounded electrode. This magnet is separated from a high-voltage powered nickel grid by a 40  $\mu\text{m}$  zirconium dioxide layer (88x27 mm, relative permittivity  $\epsilon_r \approx 27$ ), which functions as a dielectric barrier. The nickel grid, laser-cut from a 50  $\mu\text{m}$  nickel foil, contains thousands of cavities arranged in four sub-structures (10x10 mm<sup>2</sup>), with cavity diameters varying from 50 to 200  $\mu\text{m}$  with a distance of 200  $\mu\text{m}$  between each cavity. A 1 mm gap separates the sub-structures. The three layers (magnet, dielectric, and nickel grid) are held together by magnetic force. This ensures that the individual components are modular and interchangeable in order to test different dielectrics or grids or simply replace defective components. The magnetic force is strong enough to hold all components securely together without affecting the discharge, because the collision frequency of the electrons is much higher than their expected gyro frequency in the magnetic field [9]. The entire assembly is sealed by a quartz cover leading to a gas flow cross section of 2 cm width and 4 mm height). This configuration permits a controlled gas flow across the cavities and provides optical access for diagnostics. For experimental reasons, the reactor is operated with the cavities pointing downwards in this work. For the sake of comparability with other works on the reactor used, the term ‘‘above the cavities’’ in the following always refers to the area outside the cavities downstream of the opening. Further details on the reactor design can be found in references [9, 12].

### 2.2. Diagnostics

TALIF is used in this work to measure atomic oxygen density distributions (see figure 1). A picosecond laser system (EKSPLA, PL2231A and PG401) consisting of a Nd:YAG laser, a high energy broadly tunable Optical Parametric Generator (OPG) and a Second Harmonic Generator (SHG) is used to generate the UV beam at a wavelength of 225.64 nm with a repetition rate of 50 Hz and a pulse duration of 30 ps. The laser output energy at a wavelength of 225 nm is 130  $\mu\text{J}$ , measured directly at the source. The beam is directed through UV mir-

rors and a lens ( $f = 500$  mm) and focused through the quartz cover of the micro cavity plasma array, forming a circular beam profile with a diameter (FWHM) of approximately 200  $\mu\text{m}$ . The reactor is mounted on a computer-controlled translation stage (Newport, VP-25XA) that allows movement in the x, y, and z directions, enabling precise adjustment of the relative position between the laser and the reactor. The Cartesian coordinate system used is also shown in Figure 1 (a). The resulting fluorescence signal, with a wavelength of 844.9 nm, is focused using a lens (Sigma, 105 mm, set to 1:1 magnification) and passed through a band-pass filter (Andover, 840FS10-50) onto the chip of an ICCD camera (Andor, iSTAR DH334T-18U-73). To prevent laser light from reaching the detector, the camera is positioned perpendicular to the beam path. Although a top-view configuration would allow simultaneous observation of the discharge, it is not used because laser scattering by the reactor’s grid and fluorescence on the dielectric surface could interfere with the actual TALIF signal. To reduce these issues, the camera is positioned in a lateral position to ensure that interfering signals from inside the cavity (dielectric or edges of the cavity) can no longer reach the detector due to shadowing. Here, the first cavity structure (200  $\mu\text{m}$ ) is fully captured, with part of the subsequent structure (150  $\mu\text{m}$ ) also in view. The interaction volume between the laser beam and the region that can be observed with the ICCD camera is marked in orange in Figure 1 highlighting the TALIF observation region. The two-dimensional image produced by the camera thus represents the y component along the beam and the z component perpendicular to the beam (marked orange in Figure 1).

To measure TALIF signals, synchronizing the fluorescence measurement with the laser is essential. This is accomplished by using a pre-trigger signal from the laser, generated 1 ms before the laser pulse, to trigger a digital delay generator (SRS, DG645). A second digital delay generator (SRS, DG645) triggered by the first is then used to achieve at least 21 ms of delay to operate on the second laser pulse after the pre-trigger from the laser is received. While it is possible to create at least 21 ms of delay with a single delay generator, in that case TALIF measurements could only be performed on every other laser pulse, reducing the acquisition rate from 50 Hz to 25 Hz. By using two delay generators it is possible to have an acquisition rate of 50 Hz because each delay generator can be programmed with a delay less than 20 ms. The second digital delay generator coordinates the timing of all other devices, including the camera acquisition, plasma operation, and waveform acquisition. The ICCD camera is synchronized to capture the fluorescence, with its gate width set to 30 ns to account for a 1-2 ns jitter created by the rel-

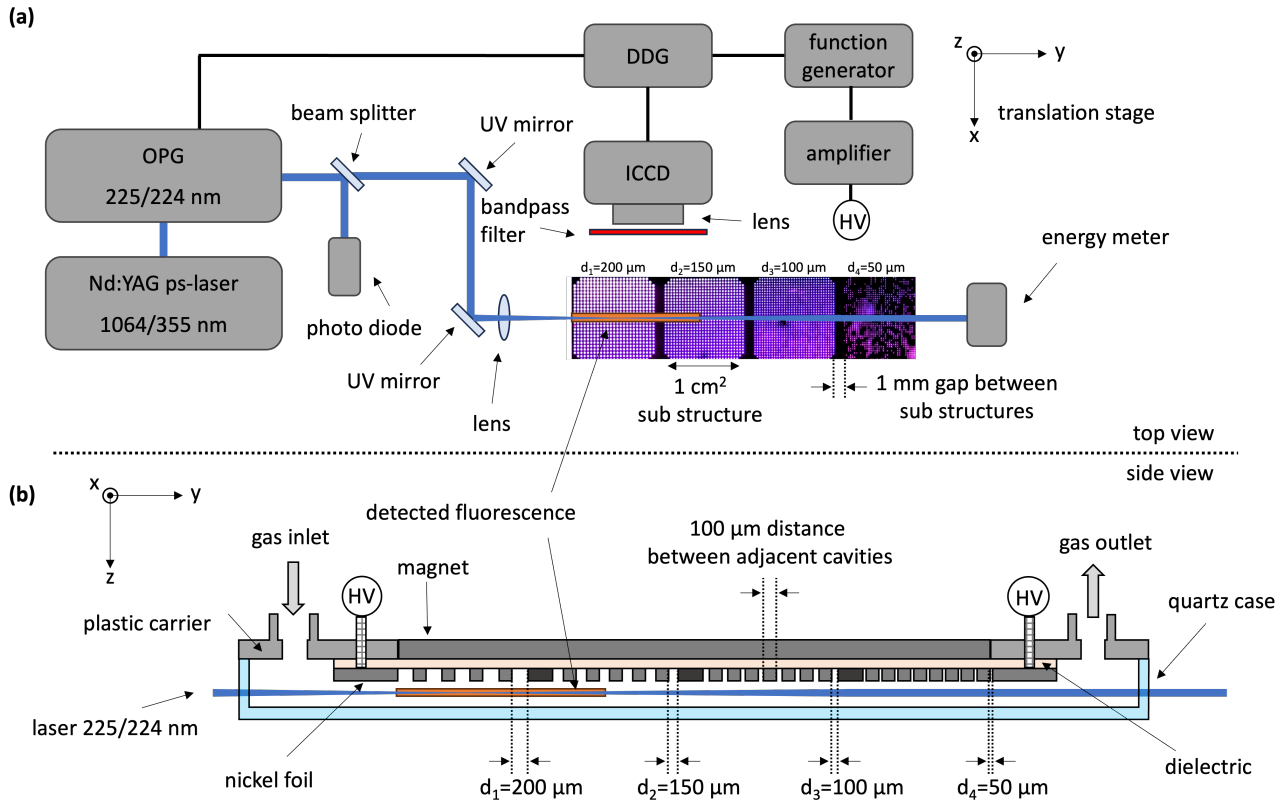


**Figure 1.** Schematic sketch of the TALIF setup and the micro cavity plasma array including the used Cartesian coordinate system.

actively long delays of the delay generators, ensuring reliable recording of the complete TALIF signal. The reactor is powered by an amplifier (Matsuda Precision AMT-1B60), which is controlled by a function generator (SRS, DS345). A sinusoidal voltage waveform with an amplitude of 700 V at 15 kHz is applied in burst mode, generating 60 pulses per trigger signal, with the voltage turned off until the next trigger. The second digital delay generator controls the start of the burst mode and the triggering of the oscilloscope (Teledyne Lecroy, HDO6104), allowing the voltage waveform to shift relative to the laser and fluorescence acquisition for temporal scanning. For the measurements, a constant gas flow of 1 slm is used and controlled by mass flow controllers (MKS, GE50A). A helium-oxygen mixture (95% helium / 5% oxygen) is available for this purpose. Pure helium can be added to fine-tune the mixture. Xenon is also available for calibration and can be mixed with helium and flowed through the micro cavity array to ensure maximum compatibility between TALIF measurements.

In addition to the density, the fluorescence signal depends quadratically on the laser intensity, which must therefore be monitored. Excessive laser energy can cause effects such as photo-dissociation, where atomic oxygen is generated by the laser itself. To prevent

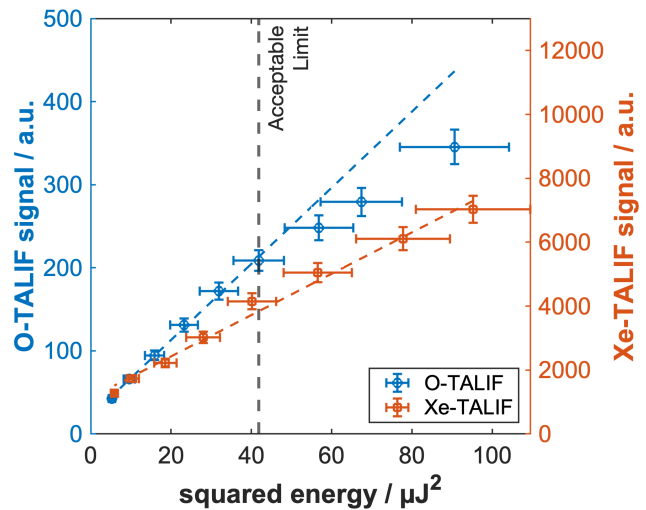


**Figure 2.** O- and Xe-TALIF signals depending on the squared laser energy. Dashed lines indicate a linear behavior. Conditions: 1 slm total gas flow (He + 0.1% O<sub>2</sub> or Xe); 700 V (for Xenon 0 V);  $z = 350 \mu\text{m}$  distance from grid surface; gate time = 30 ns; exposure time = 60 s for O and 10 s for Xe.

these effects, the laser energy can be adjusted via the laser's amplification and tracked with an energy meter (Newport 1919-R) behind the array reactor (see Figure 1). Figure 2 shows a measurement in which the

oxygen fluorescence signal was plotted as a function of the squared laser energy. For each measurement point, the energy of the laser was averaged over 1000 samples. The standard deviation of the measured energy is less than 15%. To estimate the uncertainty of the TALIF signal, 10 measurements were carried out each under the same conditions, with the standard deviation being lower than 6% (see errorbars in Figure 2). The expected behavior is a linear relationship between the TALIF signal and the squared energy. Deviations from this linearity indicate the occurrence of undesired effects, such as saturation, photo dissociation, and photo ionization, rendering the applied rate model invalid. The measurement shown here clearly indicates that there is a linear range between 5 and  $42 \mu\text{J}^2$ , which refers to a non-depletion regime. At energies above  $42 \mu\text{J}^2$ , saturation occurs, which is due to the undesirable effects described above. In order to find a compromise between high fluorescence signals and ensuring a linear behavior, energies below  $7 \mu\text{J}$  (measured in front of the array reactor with the photo diode) were used for all measurements shown in this work, which corresponds to a square energy of about  $40 \mu\text{J}^2$  (measured behind the array reactor with the energy meter). The linear behavior was checked daily, whereby day-to-day changes were negligible. In addition, the measurement was carried out with xenon (see Figure 2), which is required for calibration. As the Xe-TALIF signals are significantly higher than O-TALIF signals, the exposure time was reduced to avoid saturation of the detector. However, no saturation effects occur here, allowing the same laser energy to be used for calibration as for oxygen measurement. Besides the energy measurement shown, the depletion of the ground state can be verified by theoretical calculations as described by *Stancu* [17]. The parameters in this work were chosen in such a way that all measurements are carried out in a non-depletion regime.

Despite the fixed laser energy setting, the intensity can vary slightly from pulse to pulse. Due to the quadratic relationship, these variations can lead to large deviations in the calculated density, requiring permanent monitoring of the intensity. To achieve this, a beam splitter directs a portion of the laser beam onto a photodiode (ThorLabs, DET10A), with the signal being read via the oscilloscope (Teledyne Lecroy, HDO6104). The oscilloscope also allows monitoring of the voltage applied to the reactor and the synchronization of the laser, camera, and voltage.

Aspects of the the setup and measurement procedure used are comparable to those described in greater detail elsewhere [22].

### 2.3. Density calibration using xenon

To calculate absolute atomic oxygen densities using the TALIF setup described above, a calibration can be performed following *Niemi et al.* [19]. Here, a comparative measurement is carried out with noble gas of known density. Xenon is commonly used for calibration when measuring oxygen. The  $\text{O}(3p^3P_{1,2,0})$  state of oxygen and the  $\text{Xe}(6p^3[3/2]_2)$  state of xenon form a highly suitable pair for this purpose [20]. Thus, the required modifications to the setup are minimal: the laser wavelength is shifted from 225.64 nm to 224.29 nm, and a different band pass filter (Andover, 834.7/1.5-68381) is used to alter the observed wavelength from 844.9 nm to 834.9 nm. Traditionally, this calibration is conducted in a vacuum chamber filled with xenon. However, in this work, xenon is directly added to the gas mixture, utilizing a helium/xenon mixture at atmospheric pressure. The mixing ratio is chosen in a way that the xenon density approximates the expected oxygen density. The atomic oxygen density  $n_O$  can then be calculated using the ratio of the fluorescence signals normalized to the square laser intensity  $S_{Xe}$  for xenon and  $S_O$  for oxygen respectively.

$$\frac{S_{Xe}}{S_O} = \frac{T_{Xe}\eta_{Xe} a_{Xe} \sigma_{Xe}^{(2)}}{T_O\eta_O a_O \sigma_O^{(2)}} \frac{n_{Xe}}{n_{O(0,J=2)}} \quad (1)$$

The transmissions of the respective filters ( $T_{Xe} = 0.480$ ,  $T_O = 0.567$ ) and the sensitivity of the ICCD camera ( $\eta_{Xe} = 0.195$ ,  $\eta_O = 0.180$ ) are considered first. The optical branching ratio  $a$  takes into account the lifetime of the excited state.

$$a = \frac{A_{ik}}{A_i + \sum_q k_q n_q} \quad (2)$$

For oxygen, the optical branching ratio was calculated for each gas mixture based on literature values [20]. For xenon, a literature value of  $a=0.003$  was used for a helium/xenon mixture at atmospheric pressure [16]. For oxygen, the effective lifetime can also be measured directly with the TALIF setup used. The gate time of the ICCD is reduced for this purpose to 3 ns and the delay between laser beam and fluorescence measurement was increased in steps of 1 ns. The time decay of the signal can be fitted exponentially to determine the effective lifetime. The results reproduce theoretically calculated values. However, since the signal is subject to significant uncertainties due to the minimum gate time of 3 ns and a jitter of 1-2 ns, only theoretically calculated values were used in this work. In the case of xenon, the lifetime is too short to determine it with the setup used. The ratio of the two-photon excitation cross sections was determined by *Niemi et al.* [20] to be  $\sigma_{Xe}^{(2)}/\sigma_O^{(2)} =$

1.9 with an overall uncertainty of 20%. The xenon density  $n_{Xe}$  can be determined directly from the gas composition. For oxygen the ground state is a triple degenerate, but the measurements are only carried out at ( $J=2$ ). The density must therefore be corrected to obtain the ground state density. The ratio  $n_{0,J=2}/n_0$  can be calculated using a Boltzmann distribution and equals 74.17% at room temperature. This is assumed as all measurements are carried out within the gas flow outside the discharge. The ratio of the photon energies  $(h\nu_{Xe}/h\nu_O)^2$  was neglected here, as it results in a value very close to 1 due to the similar wavelengths. To reduce the uncertainty of this calibration, the measurement was carried out for different xenon densities.

The cross section ratio used above is only applicable for spectrally integrated signals. Since the measurements are to be conducted at a single wavelength, the calibration must be corrected. To do this, the laser wavelength can be varied in 2 pm increments to scan along the excitation. For calculating the spectral correction factor, the spectrally integrated signal is divided by the maximum signal. For the measurements, only the wavelength corresponding to the maximum signal is used, and is corrected with the calculated factor. The wavelength scan shows that the measurement is primarily dominated by the instrument profile of the laser (38 pm FWHM). Therefore, it is not possible to resolve the three oxygen sub-transitions or to calculate a Doppler temperature. Nevertheless, the wavelength scans are helpful for identifying the maximum signal, which can vary slightly from day to day (e.g. due to temperature or humidity).

As previously mentioned, the ICCD camera records a two-dimensional signal, which is influenced by the laser beam and the atomic oxygen density. When the density is spatially uniform, this results in a signal that fully illuminates the chip in the y-direction (along the laser's propagation path) and is shaped by the beam's profile width in the z-direction. Depending on the specific measurement, different parts of this imaged signal can be selected for analysis. To maximize the signal-to-noise ratio, it is advantageous to use as much of the fluorescence image as possible. However, spatial resolution can be improved by only using specific areas of the image, reducing the signal amplitude. Therefore, the evaluation of the xenon calibration is adapted to the selected signal, ensuring consistent use of the sensor regions.

The density calibration was performed several times and the results did not vary more than 10%, which shows a good stability of the system. If the constants used are taken into account, the overall density uncertainty in this work is in the order of 50%. However, it should be noted that the discussion about

the ratio of the two-photon excitation cross sections is ongoing in the diagnostics community. The value of 1.9 used in this work was recently confirmed by *Shu et al.* [24]. On the other hand, *Wubs et al.* [23] recently used a value of 1.02 based on the works of *Bamford et al.* [25] and *Drag et al.* [26] and were able to show a good agreement between THz absorption spectroscopy and TALIF measurements. Accordingly, the choice of cross section ratios can influence the calculated densities by a further factor of 2.

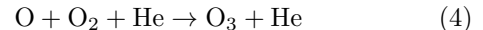
### 3. Basic diffusion model

A basic model is to be developed to compare and verify the measurements. Unlike other reactors designed for conversion, the gas flow in the micro cavity plasma array does not pass directly through the active discharge volume. Instead, a laminar gas flow is assumed between the metal grid and the quartz cover, though the efficiency of gas exchange with the cavity volume remains uncertain. Since reactive species are generated within the cavities [15], diffusion or similar mechanisms are needed to transport these species into the gas flow volume.

Diffusion can be described using Fick's second law. The change in density is described by the diffusion coefficient  $D$ . For atomic oxygen, the value is  $1.29 \times 10^{-4} \text{ m}^2 \text{ s}^{-1}$  [27].

$$\frac{\partial n}{\partial t} = D \Delta n \quad (3)$$

For a helium-oxygen mixture, the primary loss reaction is ozone formation [27]:



This can be described with a loss term  $\lambda$ , where  $k_L = 3.0 \times 10^{-46} (300/T_g^{2.6}) \text{ m}^6 \text{ s}^{-1}$  [28, 29] is the reaction rate. The density of helium  $n_{He}$  and molecular oxygen  $n_{O_2}$  are assumed to be constant.

$$\lambda = k_L n_{O_2} n_{He} \quad (5)$$

The external gas flow parallel to the reactor grid (in the y direction) can be characterized by a constant velocity  $v_y$  (for a 1 slm gas flow and an  $80 \text{ mm}^2$  cross-section,  $v_y = 0.21 \text{ m/s}$ ). Given the spatial extent of the array and that the TALIF measurements presented later were captured in two dimensions, it is reasonable to also calculate the diffusion model in two dimensions (y and z directions).

$$\frac{\partial n}{\partial t} = D_y \frac{\partial^2 n}{\partial y^2} + D_z \frac{\partial^2 n}{\partial z^2} - \lambda n - v_y \frac{\partial n}{\partial y} \quad (6)$$

This partial differential equation was solved using the explicit finite difference numerical method. A

starting density, such as a measured value, can be set as the boundary condition at  $z = 0$  (the transition between cavities and the region above). To account for time dependencies or differences between half phases of the applied voltage waveform (increasing potential phase or decreasing potential phase) of the cavities [9, 10, 12, 15], this boundary condition can vary over time. At the remaining edges, the density is set to  $n = 0$ . To avoid distortion from the boundary conditions, the model range can be extended in the  $y$  and  $z$  directions, and only the central area of the result is used for analysis. Periodic boundary conditions are not suitable due to the gas flow and additional cavity structures in the  $y$  direction. A grid with 540 points in the  $y$  direction (covering 13.3 mm) is used, with 500 points within the evaluated area and 20 points on each side ignored due to boundary conditions. In the  $z$  direction, 100 points cover 5 mm. About one million time steps of 0.1  $\mu\text{s}$  are needed for convergence.

This basic diffusion model captures the dominant effects in the region above the cavities but has limitations. Some aspects are neglected, so the results offer only a rough estimate of the density distribution and require critical review. In a more advanced model, the boundary conditions would need further refinement. For instance, the cavities and metal grid not only generate atomic oxygen but also bind it to surfaces, a loss channel that is currently ignored. Additionally, the model assumes a constant temperature over the volume, overlooking the significant temperature gradient between the cavities and the surrounding volume [15].

The chemical model is also simplified, considering only one loss reaction, whereas many reactions could contribute to O, O<sub>2</sub>, or O<sub>3</sub> dynamics. The assumption of a constant gas composition above the cavities is more reasonable than within the plasma volume, but local and temporal changes in O<sub>2</sub> and O<sub>3</sub> concentrations may still occur. Finally, the model simplifies the problem to two dimensions ( $y$  and  $z$ ), whereas, in reality, the cavities interact in three dimensions. The presence or absence of additional cavities in the  $x$  direction could further influence the density above the cavities. Finally, the model neglects possible (plasma) effects outside the discharge volume since the discharge can ignite slightly outside the cavity, especially in the increasing potential phase [9, 10]. However, including these effects would significantly complicate the model and exceed the scope of this work.

## 4. Results

### 4.1. Temporal build-up and decay of atomic oxygen

To synchronize the laser system with the discharge, a pre-trigger signal from the laser initiates the

voltage waveform at the reactor. As a result, continuous waveforms cannot be used for time resolved measurements above the cavities. Instead, a burst mode is employed with a frequency of 15 kHz and a total of 60 voltage periods. Since the discharge is off between bursts, it's important to establish when the discharge has reached steady state conditions. To verify this, TALIF measurements are taken as close as possible to the electrode without causing scattering effects (laser beam centered at a distance of  $z = 350 \mu\text{m}$  above the surface). The delay between each measurement within a burst cycle (4.1 ms) is shifted by 135  $\mu\text{s}$  to monitor changes in density. The images of fluorescence signals captured by the ICCD camera are averaged over the laser beam area to obtain a single data point. This method improves the signal-to-noise ratio but reduces local resolution in the  $z$  direction (approximately 150  $\mu\text{m}$  FWHM).

The results are presented in Figure 3 (top) for three different oxygen admixtures as a function of time (dots). For context, the corresponding voltage waveform is shown in Figure 3 (bottom). Since the density is measured outside the cavity and diffuses over time, the diffusion model described earlier can be applied in one dimension ( $z$  direction) over time at the position  $z = 350 \mu\text{m}$ . The model's solution for each admixture is also displayed in Figure 3 (top, lines). Both, the measurements and the model were normalized for easier comparison, though the discussion of absolute densities will follow in the next sections.

The model effectively replicates the basic behavior observed in the measurements. When the voltage is applied, the density above the cavities rises rapidly until it reaches steady state. Higher admixtures lead to faster saturation, which is achieved within 3 ms regardless of the admixture used. In later measurements, a fixed delay of 3.8 ms is chosen to ensure measurements under steady state conditions. When the voltage is turned off, the density decreases exponentially, as expected, due to atomic oxygen reacting with molecular oxygen to form ozone mainly. The higher the admixture, the quicker the decline.

To better compare the measurement with the model, the data can be fitted with an exponential function to determine the time constant for the buildup or decay of atomic oxygen. These time constants can then be compared to the diffusion model results (see Figure 4). The error bars represent the fit's uncertainty. As seen before, the time constants for both buildup and decay decrease with increasing admixture. This can be explained by the fact that the loss channel to ozone increases with increasing molecular oxygen admixture. In the buildup case, a balance between diffusing atomic oxygen and formation of ozone can be

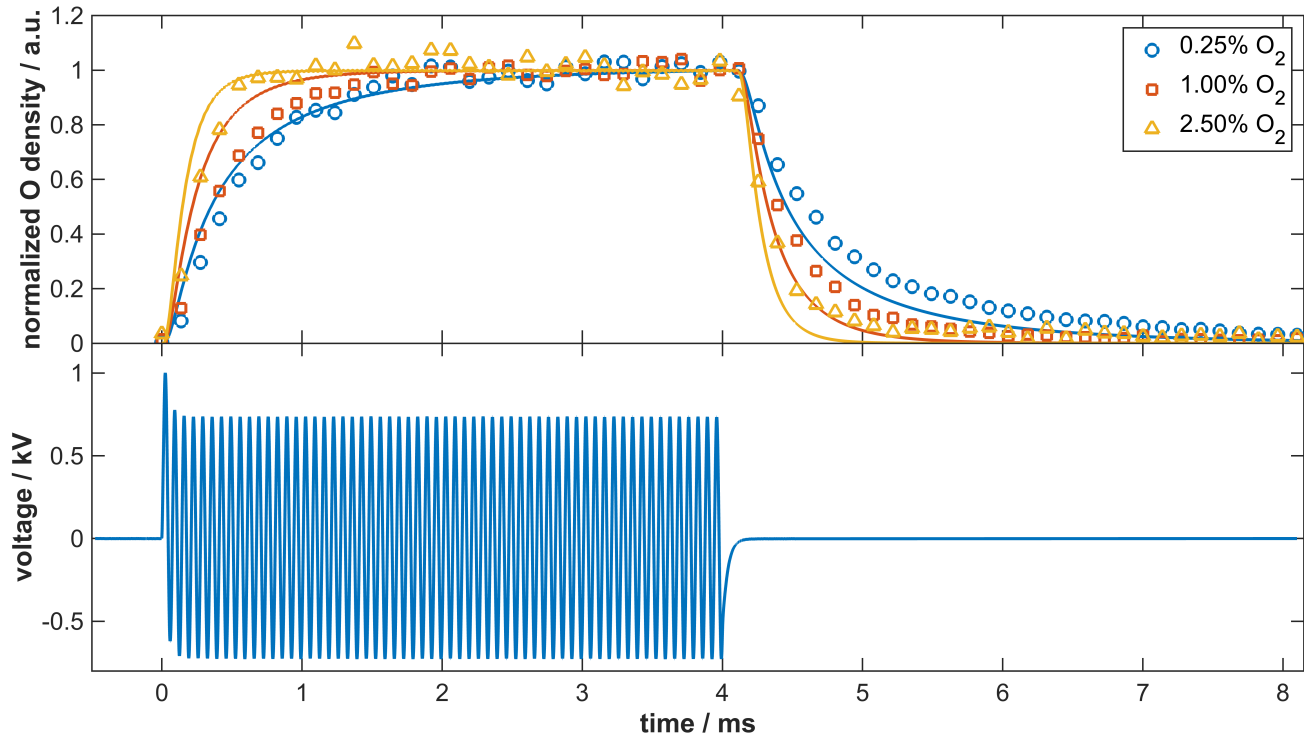


**Figure 3.** Measured (dots) and modeled (lines) atomic oxygen density for different O<sub>2</sub> admixtures depending on time (top) and voltage waveform (bottom). Conditions: 1 slm total gas flow (He+O<sub>2</sub>); 700 V amplitude;  $d = 200 \mu\text{m}$  cavity diameter;  $z = 350 \mu\text{m}$  distance from grid surface; gate time = 30 ns; total exposure time = 60 s.

achieved more quickly with a higher admixture. In the case of decay, the entire process can be described by the loss channel ozone.

Overall, the model agrees well with the measurements,

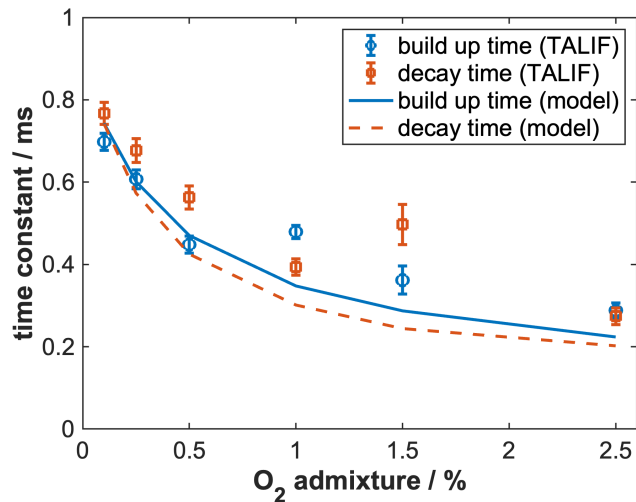


**Figure 4.** Measured (dots) and modeled (lines) build up and decay time constants depending on O<sub>2</sub> admixture. Conditions: 1 slm total gas flow (He+O<sub>2</sub>); 700 V amplitude;  $d = 200 \mu\text{m}$  cavity diameter;  $z = 350 \mu\text{m}$  distance from grid surface; gate time = 30 ns; total exposure time = 60 s.

with both the curve shapes and the absolute time

constants (200-800  $\mu\text{s}$ ) aligning well. However, the measured time constants are slightly higher than those predicted by the model, suggesting that the model may overestimate the loss term (ozone formation). As mentioned earlier, the assumption of a constant gas composition might not fully reflect reality, as other sources of atomic oxygen and ozone may be neglected. Additionally, simplifying the model to one dimension introduces errors, since adjacent cavities in  $x$  and  $y$  directions may impact the density and build up and decay times at the measurement location.

Beyond the previously discussed aspects, it's notable that neither the measurements nor the model show any modulation depending on the 15 kHz frequency used. While the waveform, especially the difference between increasing potential phase and decreasing potential phase, significantly affects conditions within the cavities [15], the TALIF measurements reveal a constant value, unaffected by the timing within the period. The model can explain this phenomenon: when the starting density (boundary condition) is periodically switched on and off (e.g., 33  $\mu\text{s}$  on, 33  $\mu\text{s}$  off), a small periodic effect is noticeable near the surface. However, this effect diminishes significantly with distance and disappears beyond  $z = 300 \mu\text{m}$ . Thus, at the measurement position of  $z = 350 \mu\text{m}$ , this influence is undetectable. Even measurements taken

closer to the surface would likely struggle to capture the periodic density changes, as the difference would be comparable to the noise level.

#### 4.2. 2D resolved density distributions above the cavities

In addition to time-resolved measurements, the setup allows for spatially resolved measurements by moving the reactor in the  $z$  direction using a translation stage. The starting point ( $z=0$ ) is where the laser is completely blocked by the reactor wall. With each step in the  $z$ -direction, more of the laser beam passes across the grid, enabling measurements directly in front of the grid surface and scanning the entire volume above the cavities. As the laser propagates in  $y$  direction, a two-dimensional density profile is obtained.

Unlike previous measurements, which averaged the entire laser width in the  $z$  direction to improve the signal-to-noise ratio, these measurements prioritize local resolution. Therefore, only a  $50\ \mu\text{m}$  section of the laser beam profile is evaluated, matching the step size of the translation stage. A schematic sketch of the area used is shown in Figure 6. To minimize scattering, reflections, and fluorescence effects when the laser is close to the surface, only the  $50\ \mu\text{m}$  section of the  $200\ \mu\text{m}$  laser or fluorescence beam nearest the surface is analyzed. While this reduces intensity (which would be higher using the beam center), it significantly decreases disturbances since the laser's center remains further from the surface at each point.

As previously discussed, the measured TALIF signal depends not only on the density to be determined, but also quadratically on the laser intensity, which is monitored using a diode (see section 2.2). This procedure allows fluctuations in the laser intensity to be corrected. However, the intensity in the volume of interest is influenced not only by the laser but also by the elements in the beam path, such as the quartz cover. In the case of  $z$ -variation, this cover is moved relative to the laser. Small defects such as scratches or contaminations then result in a position-dependent intensity profile that cannot be corrected by the diode. To address this, a calibration measurement with xenon can be performed. The same  $z$ -scan used for atomic oxygen is conducted, substituting xenon for oxygen in the helium flow and adjusting the laser to  $224.29\ \text{nm}$ . The bandpass filter is wide enough and doesn't need changing for this measurement. Since xenon density can be assumed as uniform with the discharge off, any variations in the TALIF signal are due to quartz cover or surface effects. The xenon measurement therefore results in a spatially resolved intensity map of the volume observed for oxygen depending on the  $z$  and  $y$  position. If this map is normalized and multiplied by the diode signal, a

two-dimensional map proportional to the position-dependent excitation intensity is obtained. This allows not only fluctuations in the laser energy but also position-dependent interference from the quartz cover or the surface to be compensated for.

The results are shown in Figure 5 (left column), with the micro cavity plasma array positioned at  $z = 0\ \text{mm}$ . The cavity openings face downward, allowing the outflow to propagate in the positive  $z$  direction. The ICCD camera's position captures both the  $200\ \mu\text{m}$  (left) and part of the  $150\ \mu\text{m}$  (right) cavity structure. Measurements are taken for three different oxygen admixtures and are calibrated to determine absolute density.

As expected, atomic oxygen density peaks around the area of the cavities and decreases exponentially above them. Initially, the oxygen density increases with more oxygen added but declines at higher admixtures. At 1.5% admixture, not all cavities ignite, leading to individual density maxima in  $y$  direction. However, the laser width is broad enough to potentially span two rows of cavities in  $x$  direction, and diffusion in the  $x$  and  $y$  directions means distant cavities can affect the measurement point. Thus, distinct structures only appear when an entire cluster of cavities fails to ignite. The results in the area of  $150\ \mu\text{m}$  diameter cavities near  $y = 12\ \text{mm}$  are consistent with those in the area of  $200\ \mu\text{m}$  diameter cavities, consistent with actinometry measurements [15], where cavity size did not measurably impact density.

The basic diffusion model results are also shown in Figure 5 (right column), using the first line of measured values ( $z = 0\ \text{mm}$ ) as the starting density. In reality, this point is approximately  $20\ \mu\text{m}$  away from the surface due to inaccuracies in the adjustment. The model closely matches the measurements, except at the lowest admixture (0.1%). At low admixtures, uncertainties in the gas flow or the premixed gas mixture have a larger impact. If the admixture were higher than assumed, this would strongly influence the model and reduce the deviation from the measurement. Moreover, the model only considers the three-body reaction between O, O<sub>2</sub>, and He as the loss term, which dominates at higher admixtures. At lower admixtures, these losses approach zero, suggesting additional loss terms might be necessary. However, this requires a complex chemical model that goes beyond the scope of this work.

Both, the measurements and the model indicate that atomic oxygen can travel a few millimeters from the cavities, which is crucial for plasma catalytic applications. Contour lines added to the model and measurements highlight their comparability, with the exponential decay matching up to densities of around  $2 \times 10^{14}\ \text{cm}^{-3}$ . Below this, the noise level (detection

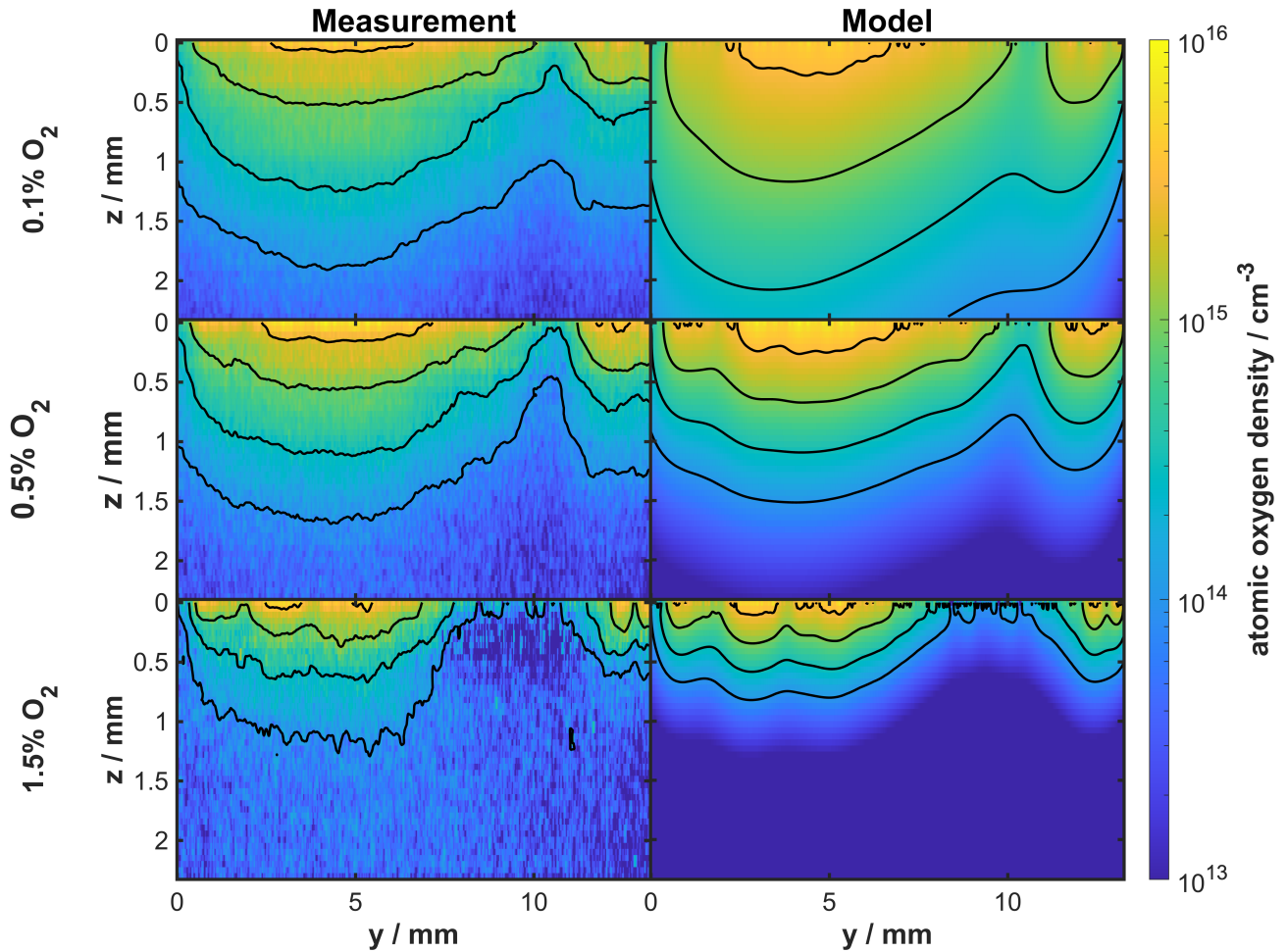


**Figure 5.** Measured (left) and modeled (right) 2d resolved atomic oxygen density for different admixtures. The cavities are located at  $z = 0$  mm. Contour lines indicate exemplary densities for the comparability of model and experiment. Conditions: 1 slm total gas flow (He+O<sub>2</sub>); 700 V amplitude;  $d = 200$   $\mu$ m (left) / 150  $\mu$ m (right) cavity diameter;  $z$ -step = 50  $\mu$ m; gate time = 30 ns; total exposure time = 60 s.

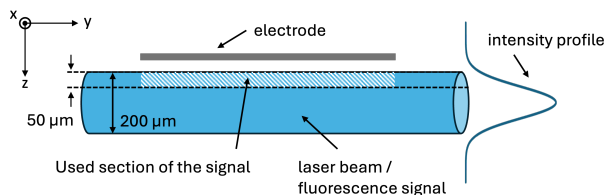


**Figure 6.** Schematic sketch of the TALIF signal and laser intensity profile used.

limit) in the measurement causes deviations.

The model also accounts for gas flow effects, though these appear minimal. This means oxygen atoms from the 150  $\mu$ m structures do not interact with the 200  $\mu$ m structures' outflow (1 mm away), preventing density accumulation. Higher flow velocities would be needed to see this effect, which could be relevant for certain applications. The gas flow effect is barely visible in

the measurements, possibly due to the limited signal-to-noise ratio. In addition, despite assuming laminar flow, the velocity near the surface is likely lower than in the rest of the volume, reducing the influence of the gas flow on the distribution of atomic density in the volume immediately above the surface.

Lastly, the influence of the voltage period is most pronounced near the surface, where the  $z$ -scans were measured. To minimize error, all measurements were taken at the same point in time at the end of the decreasing potential phase, where oxygen production is expected to peak [15]. Measurements during the increasing potential phase are not possible, as the discharge ignites outside the cavity [10], interfering with the results.

#### 4.3. Dependence on gas composition and comparison with results within cavities

The impact of admixture on the volume above the cavities, particularly due to the reaction leading to ozone formation, has been previously discussed. This section delves deeper into that analysis. As before, measurements are taken at a fixed position above the cavities ( $z = 350 \mu\text{m}$ ) while varying the admixture, followed by absolute calibration. Since high admixture levels cause some cavities to fade, potentially distorting the density measurements above the cavities, the number of ignited cavities near the laser beam is counted for each admixture, and the measurements are corrected accordingly.

The results are presented in Figure 7, with error

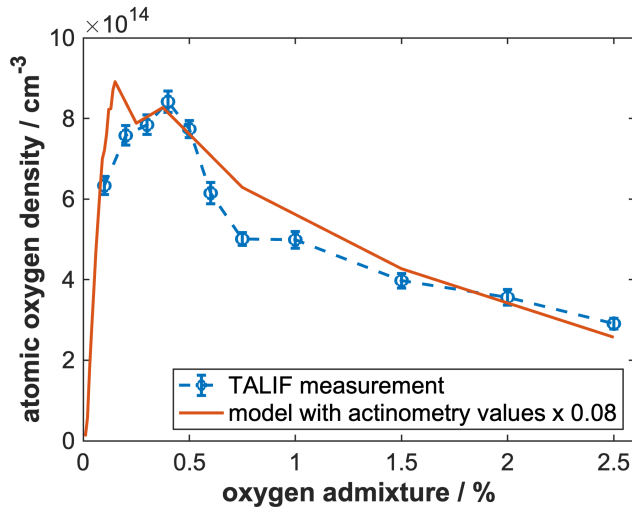


**Figure 7.** Admixture variation for TALIF measurement compared to basic diffusion model based on actinometry measurements. A correction factor of 0.08 is applied to account for the surface losses neglected in the model. Conditions: 1slm total gas flow (He+O<sub>2</sub>); 700 V amplitude;  $d = 200 \mu\text{m}/150 \mu\text{m}$  cavity diameter;  $z = 350 \mu\text{m}$  distance from grid surface; gate time = 30 ns; total exposure time = 60 s.

bars representing the standard deviation of ten measurements. Initially, density rises with increasing admixture, peaking at  $8.4 \times 10^{14} \text{ cm}^{-3}$  around 0.4% admixture. Beyond that, density decreases, dropping to  $2.9 \times 10^{14} \text{ cm}^{-3}$  at 2.5% admixture. These absolute densities are consistent with the  $z$ -scans discussed earlier. Small deviations are due to the fact that in this case the density was averaged along the entire laser or fluorescence beam above a row of the array structure, whereas in the  $z$  scans each  $y$  value was evaluated individually.

The result differs significantly from previous helium state enhanced actinometry (SEA) measurements inside the cavity, where a continuous increase in density was observed with the addition of oxygen [15] (not shown here). This deviation can be addressed using the

basic diffusion model. By using the actinometry measurements as the initial density within the cavity and applying the model to the region above the cavities, the density dependence curve can be closely matched. Further refinement is possible by incorporating actual discharge times, i.e., switching the source on and off (see Figure 7).

The difference between the cavities and the area above them can be explained as follows: Inside the cavity, molecular oxygen can be almost completely dissociated. Consequently, increasing the admixture results in a higher density. However, as atomic oxygen diffuses out of the cavity, it encounters molecular oxygen and forms ozone. With higher admixture, this loss becomes dominant. At 0.4% admixture, an optimum is reached between production and loss.

Despite the close match of the curves, a correction factor of 0.08 is needed to align the absolute densities. This discrepancy arises from several factors: Actinometry measurements only account for the ignited cavities, whereas the density above the cavities involves the 3D interaction of multiple (potentially non-ignited) cavities. Even if all cavities were ignited, the ratio of cavity area to electrode area is just 20%, considering the total area of the array structure ( $1 \times 1 \text{ cm}^2$ ) in relation to the sum of the individual cavity sizes, significantly reducing the actual density above the cavities.

Additionally, actinometry does not specify the  $z$  position of the generated density, as spatial integration is performed in this direction. The model assumes the density is at the bottom of the cavity, but the discharge volume and location vary between the voltages half phases [10]. Moreover, absolute densities from actinometry should generally be critically questioned [14]. Another source of error is the model itself. Surface losses are completely ignored here. However, these will be maximum within the cavity surrounded by the electrode and dielectric, raising the question of how much of the oxygen generated in the cavity can actually leave it.

Despite these uncertainties, this result provides a valuable benchmark for the actinometry measurements. The density curves from TALIF and SEA are nearly identical, with deviations primarily attributed to surface losses or the cavity-to-electrode area ratio. Overall, the phenomena above the cavities can be effectively described using the discharge dynamics determined within the cavities in combination with diffusion and the formation of ozone.

## 5. Conclusion

Atomic oxygen densities in the volume above a micro cavity plasma array were successfully determined using TALIF measurements and explained by a basic

model. The results indicate that this region is dominated by diffusion and ozone formation. Time-resolved measurements show that equilibrium is reached near the cavities within 3 ms (depending on the admixture, it can occur even sooner). This knowledge is crucial for optimizing the reactor, especially for plasma-catalytic applications involving gas reactions and surface interactions. For instance, the voltage waveform could be tailored or the geometry modified for faster conversion. Spatially resolved measurements confirm these findings, showing that the gas flow has a negligible impact on the transport of atomic oxygen. To achieve accumulation from cavity to cavity, the flow velocity would need to be increased, either by adjusting the flow rate or by reducing the cross-sectional area between the quartz cover and metal grid. Furthermore, the study reveals that atomic oxygen can escape from the cavities by several millimeters, which is again beneficial for potential applications.

A variation in the admixture shows optimal dissociation at 0.4%, where there is a balance between production inside the cavity and losses outside. The basic diffusion model links earlier measurements within the cavities to the area above, demonstrating that the dynamics of reactive species throughout the reactor can be explained by understanding the dynamics within the cavities. Additionally, the significant interaction with the surface (surface losses of oxygen) is highlighted, which is valuable for future applications, as surfaces could be coated with a catalytic layer that directly interacts with the reactive species.

Overall, this study reinforces that the micro cavity plasma array reactor provides optimal conditions for plasma-catalytic applications. Reactive species are generated at high densities within the cavities and diffuse several millimeters outward. Although the production and loss processes might differ for more complex gases like carbon dioxide, it can be assumed that the fundamental dynamics are comparable to the model system of oxygen. With this understanding, the reactor can be further optimized in the future, for example, by improving gas exchange within the cavities, optimizing transport to surfaces, or increasing energy efficiency to achieve the goal of plasma catalysis.

## Acknowledgments

This project is supported by the DFG in the frame of the CRC 1316 project A6, the Ruhr University Research School [DFG GSC 98/3], and by Sandia National Laboratories' Plasma Research Facility, funded by the U.S. Department of Energy Office of Fusion Energy Sciences, and by Award Number DESC0020232. Sandia is managed and operated by NTESS under DOE NNSA contract DE-

NA0003525.

## 6. References

- [1] Ashford B and Tu X 2017 *Current Opinion in Green and Sustainable Chemistry* **3** 45–49 ISSN 24522236 URL <https://linkinghub.elsevier.com/retrieve/pii/S245222361630061X>
- [2] Snoeckx R and Bogaerts A 2017 *Chemical Society Reviews* **46** 5805–5863 ISSN 0306-0012, 1460-4744 URL <https://xlink.rsc.org/?DOI=C6CS00066E>
- [3] George A, Shen B, Craven M, Wang Y, Kang D, Wu C and Tu X 2021 *Renewable and Sustainable Energy Reviews* **135** 109702 ISSN 13640321 URL <https://linkinghub.elsevier.com/retrieve/pii/S1364032120300010>
- [4] Bogaerts A, Tu X, Whitehead J C, Centi G, Lefferts L, Guitella O, Azzolina-Jury F, Kim H H, Murphy A B, Schneider W F, Nozaki T, Hicks J C, Rousseau A, Thevenet F, Khacef A and Carreon M 2020 *Journal of Physics D: Applied Physics* **53** 443001 ISSN 0022-3727, 1361-6463 URL <https://iopscience.iop.org/article/10.1088/1361-6463/ab9048>
- [5] Hinde P, Demidyuk V, Gkelios A and Tipton C 2020 *Johnson Matthey Technology Review* **64** 138–147 ISSN 2056-5135 URL <https://www.ingentaconnect.com/content/10.1595/205651320X15759961130711>
- [6] Van Durme J, Dewulf J, Leys C and Van Langenhove H 2008 *Applied Catalysis B: Environmental* **78** 324–333 URL <https://linkinghub.elsevier.com/retrieve/pii/S0926337307003037>
- [7] Whitehead J C 2016 *Journal of Physics D: Applied Physics* **49** 243001 ISSN 0022-3727, 1361-6463 URL <https://iopscience.iop.org/article/10.1088/0022-3727/49/24/243001>
- [8] Jiang J and Bruggeman P J 2021 *Journal of Physics D: Applied Physics* **54** 214005 ISSN 0022-3727, 1361-6463 URL <https://iopscience.iop.org/article/10.1088/1361-6463/abe89a>
- [9] Dzikowski S, Michaud R, Böttner H, Dussart R, Böke M and Schulz-von der Gathen V 2020 *Plasma Sources Science and Technology* **29** 035028 URL <https://iopscience.iop.org/article/10.1088/1361-6595/ab71f6>
- [10] Kreuznacht S, Böke M and Schulz-von der Gathen V 2021 *Plasma Sources Science and Technology* **30** 015014 URL <https://iopscience.iop.org/article/10.1088/1361-6595/abd61e>
- [11] Labenski R, Steuer D, Van Impel H, Böke M, Schulz-von Der Gathen V and Golda J 2024 *Plasma Sources Science and Technology* **33** 105022 ISSN 0963-0252, 1361-6595 URL <https://iopscience.iop.org/article/10.1088/1361-6595/ad802d>
- [12] Dzikowski S, Steuer D, Iséni S, Golda J, Böke M and Schulz-von der Gathen V 2022 *Plasma Sources Science and Technology* **31** 065014 ISSN 0963-0252, 1361-6595 URL <https://iopscience.iop.org/article/10.1088/1361-6595/ac7820>
- [13] Van Impel H, Steuer D, Labenski R, Schulz-von Der Gathen V, Böke M and Golda J 2024 *Plasma Sources Science and Technology* **33** 105008 ISSN 0963-0252, 1361-6595 URL <https://iopscience.iop.org/article/10.1088/1361-6595/ad7d34>
- [14] Steuer D, van Impel H, Gibson A R, Schulz-von der Gathen V, Böke M and Golda J 2022 *Plasma Sources Science and Technology* **31** 10LT01 URL <https://iopscience.iop.org/article/10.1088/1361-6595/ac90e8>
- [15] Steuer D, Van Impel H, Schulz-von der Gathen V, Böke M and Golda J 2023 *Plasma Sources Science and Technology* **32** 025013 ISSN 0963-0252, 1361-

- 6595 URL <https://iopscience.iop.org/article/10.1088/1361-6595/acb9b9>
- [16] Van Gessel A F H, Van Grootel S C and Bruggeman P J 2013 *Plasma Sources Science and Technology* **22** 055010 ISSN 0963-0252, 1361-6595 URL <https://iopscience.iop.org/article/10.1088/0963-0252/22/5/055010>
- [17] Stancu G D 2020 *Plasma Sources Science and Technology* **29** 054001 ISSN 1361-6595 URL <https://iopscience.iop.org/article/10.1088/1361-6595/ab85d0>
- [18] Steuer D, Korolov I, Chur S, Schulze J, Schulz-von der Gathen V, Golda J and Böke M 2021 *Journal of Physics D: Applied Physics* **54** 355204 ISSN 0022-3727, 1361-6463 URL <https://iopscience.iop.org/article/10.1088/1361-6463/ac09b9>
- [19] Niemi K, Schulz-von der Gathen V and Döbele H F 2001 *Journal of Physics D: Applied Physics* **34** 2330 URL <https://iopscience.iop.org/article/10.1088/0022-3727/34/15/312>
- [20] Niemi K, Schulz-von der Gathen V and Döbele H F 2005 *Plasma Sources Science and Technology* **14** 375 URL <https://iopscience.iop.org/article/10.1088/0963-0252/14/2/021>
- [21] Klose S J, Ellis J, Riedel F, Schröter S, Niemi K, Semenov I L, Weltmann K D, Gans T, O'Connell D and Van Helden J H 2020 *Plasma Sources Science and Technology* **29** 125018 ISSN 0963-0252, 1361-6595 URL <https://iopscience.iop.org/article/10.1088/1361-6595/abcc4f>
- [22] Myers B, Barnat E and Stapelmann K 2021 *Journal of Physics D: Applied Physics* **54** 455202 ISSN 0022-3727, 1361-6463 URL <https://iopscience.iop.org/article/10.1088/1361-6463/ac1cb5>
- [23] Wubs J R, Invernizzi L, Gazeli K, Macherius U, Lü X, Schrottke L, Lombardi G, Weltmann K D and Van Helden J H 2023 *Applied Physics Letters* **123** 081107 ISSN 0003-6951, 1077-3118 URL <https://pubs.aip.org/apl/article/123/8/081107/2907730/Validation-of-THz-absorption-spectroscopy-by-a>
- [24] Shu Z, Popov N A and Starikovskaia S M 2024 *Plasma Sources Science and Technology* **33** 025019 ISSN 0963-0252, 1361-6595 URL <https://iopscience.iop.org/article/10.1088/1361-6595/ad270f>
- [25] Bamford D J, Jusinski L E and Bischel W K 1986 *Physical Review A* **34** 185–198 ISSN 0556-2791 URL <https://link.aps.org/doi/10.1103/PhysRevA.34.185>
- [26] Drag C, Marmuse F and Blondel C 2021 *Plasma Sources Science and Technology* **30** 075026 URL <https://iopscience.iop.org/article/10.1088/1361-6595/abfbcb>
- [27] Waskoenig J, Niemi K, Knake N, Graham L M, Reuter S, Schulz-von der Gathen V and Gans T 2010 *Plasma Sources Science and Technology* **19** 045018 URL <https://iopscience.iop.org/article/10.1088/0963-0252/19/4/045018>
- [28] Stafford D S and Kushner M J 2004 *Journal of Applied Physics* **96** 2451–2465 ISSN 0021-8979, 1089-7550 URL <https://pubs.aip.org/jap/article/96/5/2451/906235/02-1-production-in-He-02-mixtures-in-flowing-low>
- [29] Turner M M 2016 *Plasma Sources Science and Technology* **25** 015003 ISSN 0963-0252, 1361-6595 URL <https://iopscience.iop.org/article/10.1088/0963-0252/25/1/015003>